AGU PUBLICATIONS

JGR

Journal of Geophysical Research: Space Physics

RESEARCH ARTICLE
10.1002/2015JA021158

Spacecraft plume interactions with the magnetosphere plasma environment in geostationary Earth orbit

K. A. Stephani[1] and I. D. Boyd[2]

[1]Department of Mechanical Science and Engineering, University of Illinois at Urbana-Champaign, Urbana, Illinois, USA, [2]Department of Aerospace Engineering, University of Michigan, Ann Arbor, Michigan, USA

Key Points:
- Spacecraft hydrazine plume interacts with GEO via charge exchange and photoionization processes
- Magnetized hydrazine ion plumes envelop spacecraft, and neutral plumes convect downstream
- Ion and neutral plume dissipation times longer and species-dependent

Correspondence to:
K. A. Stephani,
ksteph@illinois.edu

Citation:
Stephani, K. A., and I. D. Boyd (2016), Spacecraft plume interactions with the magnetosphere plasma environment in geostationary Earth orbit, *J. Geophys. Res. Space Physics*, *121*, 1402–1412, doi:10.1002/2015JA021158.

Received 24 FEB 2015
Accepted 1 FEB 2016
Accepted article online 3 FEB 2016
Published online 27 FEB 2016

Abstract Particle-based kinetic simulations of steady and unsteady hydrazine chemical rocket plumes are presented in a study of plume interactions with the ambient magnetosphere in geostationary Earth orbit. The hydrazine chemical rocket plume expands into a near-vacuum plasma environment, requiring the use of a combined direct simulation Monte Carlo/particle-in-cell methodology for the rarefied plasma conditions. Detailed total and differential cross sections are employed to characterize the charge exchange reactions between the neutral hydrazine plume mixture and the ambient hydrogen ions, and ion production is also modeled for photoionization processes. These ionization processes lead to an increase in local plasma density surrounding the spacecraft owing to a partial ionization of the relatively high-density hydrazine plume. Results from the steady plume simulations indicate that the formation of the hydrazine ion plume are driven by several competing mechanisms, including (1) local depletion and (2) replenishing of ambient H^+ ions by charge exchange and thermal motion of 1 keV H^+ from the ambient reservoir, respectively, and (3) photoionization processes. The self-consistent electrostatic field forces and the geostationary magnetic field have only a small influence on the dynamics of the ion plume. The unsteady plume simulations show a variation in neutral and ion plume dissipation times consistent with the variation in relative diffusion rates of the chemical species, with full H_2 dissipation (below the ambient number density levels) approximately 33 s after a 2 s thruster burn.

1. Introduction

Spacecraft in orbit use thruster burns for orbital maneuvers including changes in orbital inclination and delta-V maneuvers. The plumes that form as a result of these burns are very high in density relative to the near-vacuum ambient environment, presenting significant challenges concerning plume impingement on spacecraft surfaces. Direct plume impingement can generate unwanted torques on the spacecraft, as well as localized heating and contamination of sensitive surfaces. Predictive capabilities to assess and mitigate plume impingement on critical spacecraft surfaces rely on models that capture the nonequilibrium nature of the plume expansion, as well as the interaction of the plume with the ambient plasma environment. Neutral postcombustion constituents in chemical rocket plumes are subject to charge-exchange interactions with the ambient space plasma, which lead to the formation of a high-density ion plume. A fundamental understanding of plume interactions with the ambient plasma is thus imperative for the characterization of plume dynamics, especially concerning plume impingement issues.

A number of experimental (laboratory and in situ) and computational studies have been conducted to assess the effects of plume interaction and impingement on spacecraft surfaces [*Burke et al.*, 1995; *McMahon et al.*, 1983; *Karabadzhak et al.*, 1997; *Drakes and Swann*, 1999; *Kaplan and Bernhardt*, 2010; *Bernhardt et al.*, 2012]. Burke et al., in particular, presented measurements of positive, single-charge ion energy distributions detected during thruster burns of the tethered satellite system 1 mission by the Shuttle Potential and Return Electron Experiment. These measurements reported energy and angular distributions of pickup ions (ions formed through charge-exchange reactions between thruster neutral particles and ambient ions) impacting the sensor. In comparison of these results to predicted ion trajectories from a collisionless two-dimensional simulation model, it was concluded that strong scattering must occur near the highly collisional thruster exit to account for the main features of the detected ion energy spectra. These studies focused primarily on the influence of the magnetic field on pickup ion trajectories and were limited to relatively short-range detection distances.

Additional computational models, including direct simulation Monte Carlo (DSMC), ray-tracing and particle-tracing methods, have been developed to aid in the prediction of plume interaction with the ambient environment and with spacecraft surfaces [*Alexeenko et al.*, 2004; *Ngalande et al.*, 2006; *Yim et al.*, 2014]. These models have been used to investigate plume contamination characteristics [*Alexeenko et al.*, 2004], surface heating due to plume impingement [*Yim et al.*, 2014], and effects of surface roughness on near-field plume development [*Ngalande et al.*, 2006]. Although these models address the collisional aspect of the plume, the studies have been largely focused on spacecraft plume interactions over relatively small distances and neglect environmental considerations from charge-exchange reactions or electrostatic and magnetic field effects. Incorporating these effects is critical for capturing the development of the spacecraft plume in the plasma environment, particularly over large distances. Recent efforts [*Stephani and Boyd*, 2014; *Stephani et al.*, 2014] investigating spacecraft plumes in low Earth orbit (LEO) have demonstrated that interaction of the spacecraft neutral plume with the ambient plasma forms a relatively high-density spacecraft ion plume. The propagation of this ion plume is determined primarily by the interaction with the magnetic field, but the development of the neutral spacecraft plume is also affected (albeit indirectly) by the magnetic field interaction owing to secondary charge-exchange reactions.

The present study aims to examine the interaction between spacecraft hydrazine thruster plumes and the ambient magnetosphere in geostationary Earth orbit (GEO) conditions. While previous efforts have developed a combined direct simulation Monte Carlo/particle-in-cell (DSMC/PIC) methodology to examine plumes in LEO [*Stephani and Boyd*, 2014; *Stephani et al.*, 2014], this study focuses on the additional physical model considerations involving nonequilibrium plasma mixtures. The rarefied nature of the magnetosphere, as well as the presence of the surrounding plasma environment, requires the use of a combined DSMC/PIC methodology, which is detailed next. The ambient conditions in the magnetosphere present an environment in which photoionization processes become comparable to charge transfer processes, contrary to the LEO environment. Results are presented for both steady and unsteady spacecraft thruster burns, in which the neutral rocket plume is modeled as a mixture of three primary propellant species. The influence of both charge transfer and photoionization processes on the development of the neutral and ion plumes are also investigated.

2. Modeling of Plume/Magnetosphere Interactions

2.1. DSMC/PIC Framework

The charge exchange collisions between ambient ions and rocket plume combustion species occur under very low density conditions. The most appropriate numerical method for simulation of these phenomena is the direct simulation Monte Carlo (DSMC) method [*Bird*, 1994]. The plasma formed in this process is subject to self-consistent electrostatic fields, which is most appropriately modeled using the particle-in-cell (PIC) method [*Birdsall and Langdon*, 2004]. The combination of rarefied collisional and plasma phenomena relevant to the physical system of interest is therefore analyzed using MPIC [*Cai*, 2005], which uses the DSMC and PIC methods simultaneously to model the flow field.

2.2. MEX/CEX Collision Dynamics and Photoionization

The ambient magnetosphere model used in this study is composed of H^+, the primary ion species found at GEO. The spacecraft thruster ejects a high-density plume of neutral particles which expands into the surrounding ambient flow. Interaction of the chemical rocket plume mixture with the ambient H^+ leads to the formation of an ion plume mixture through charge exchange (CEX) reactions. The chemical system under consideration is thus composed of seven chemical species: the ambient H^+ ions, the hydrazine combustion products, H_2, N_2, and NH_3, and their corresponding ions, H_2^+, N_2^+, and NH_3^+.

The ambient H^+ ions are allowed to participate in both momentum exchange (MEX) and CEX interactions with the plume constituents, but the postcollision properties of H^+ are updated in order to simulate the local depleting/replenishing of H^+ in the vicinity of the spacecraft plume. The ambient H^+ ions are depleted upon charge exchange with spacecraft neutral particles, forming neutral H atoms, but the surrounding ambient provides an infinite reservoir of H^+ ions at 1 keV to replenish the local population. This replenishing process is modeled as a finite-rate reactivation of ambient H neutrals to ions. The rate of reactivation is based on the time-of-flight for a 1 keV H^+ ion to reach the position of the H neutral from an infinite reservoir at $x = -20$ km. As will be seen in the steady state simulation results, the infinite reservoir is taken at the $x-$location where the steady state neutral plume density falls off below the ambient density.

Table 1. VHS Parameters for $H_2/N_2/NH_3$

	d_{ref}	T_{ref}	ω
H_2	2.92 Å	273 K	0.75
N_2	4.17 Å	273 K	0.75
NH_3	5.94 Å	273 K	0.75

Photoionization processes involving the ionization of spacecraft neutrals are also included in this model. The photoionization collision frequency is based on integration of the product of the photoionization cross section with Planck's spectral black-body emissive power with respect to wavelength. The resulting collision frequencies employed in these calculations are $O(1 \times 10^{-6})$ collisions per second.

All of the chemical species comprising the spacecraft plume mixture participate in MEX/CEX interactions, and binary collisions and postcollision scattering are computed based on detailed total and differential cross sections. The rotational, vibrational, and electronic internal structure of plume constituents is currently neglected in this work.

The collision details involving plasma mixtures requires a careful treatment for collisions between neutral and charged particles, particularly in cases where the collision partners are not like species. Within the DSMC method, collision dynamics are imposed in the center-of-mass frame of reference of the colliding particles. Collisions involving two neutral particles are processed using the variable hard sphere (VHS) model, in which the probability of a collision is computed according to

$$P = \frac{\sigma g}{(\sigma g)_{\max}}, \tag{1}$$

where σ is the total cross section and g is the relative collision speed, and a candidate pair is selected for collision if $P > \mathcal{R}_u$, where $\mathcal{R}_u$ is a uniformly distributed random number. Heavy particle interactions are treated according to standard DSMC collision dynamics, with the possibility of a charge transfer for neutral/ion collision pairs. The total number of candidate collision partners within a cell is determined using Bird's No-Time-Counter [*Bird*, 1994] method. The probability of a collision event is then determined for these candidate pairs based on the total collision cross section. MEX collisions for neutral particle interactions are modeled using variable hard sphere [*Bird*, 1994] (VHS) total cross sections and isotropic scattering. The corresponding VHS parameters including the reference diameter d_{ref}, reference temperature T_{ref}, and temperature exponent ω for the gas mixture constituents are provided in Table 1.

Postcollision velocities involving neutral collision pairs are assumed to follow isotropic scattering in the center-of-mass frame of reference. Collisions involving neutral/ion pairs, however, scatter anisotropically, with a strong forward scattering tendency. Total and differential cross section data for this system are obtained from the literature [*Kusakabe et al.*, 2000; *Cabrera-Trujillo et al.*, 2002; *Coplan and Ogilvie*, 1970] for both direct and charge transfer collisions based on guided ion beam experimental results and the electron nuclear dynamics formalism. While the total cross section is invariant under transformation of reference frame, the differential cross section must be converted from the laboratory (LAB) reference frame to the center-of-mass (CM) reference frame for use within the DSMC/PIC framework. The differential cross section (DCS) transformation is established through the relationship between the LAB and CM total cross-sectional area:

$$\frac{d\sigma(\theta_{CM})}{d\Omega_{CM}} d\Omega_{CM} = \frac{d\sigma(\theta_{LAB})}{d\Omega_{LAB}} d\Omega_{LAB} \tag{2}$$

where

$$d\Omega_{CM} = 2\pi \sin(\theta_{CM}) d\theta_{CM}, \tag{3}$$

$$d\Omega_{LAB} = 2\pi \sin(\theta_{LAB}) d\theta_{LAB}. \tag{4}$$

For a LAB → CM transformation, equation (2) is written as follows:

$$\frac{d\sigma(\theta_{CM})}{d\Omega_{CM}} = \frac{d\sigma(\theta_{LAB})}{d\Omega_{LAB}} \frac{d\Omega_{LAB}}{d\Omega_{CM}} = \frac{d\sigma(\theta_{LAB})}{d\Omega_{LAB}} \frac{\sin(\theta_{LAB}) d\theta_{LAB}}{\sin(\theta_{CM}) d\theta_{CM}} \tag{5}$$

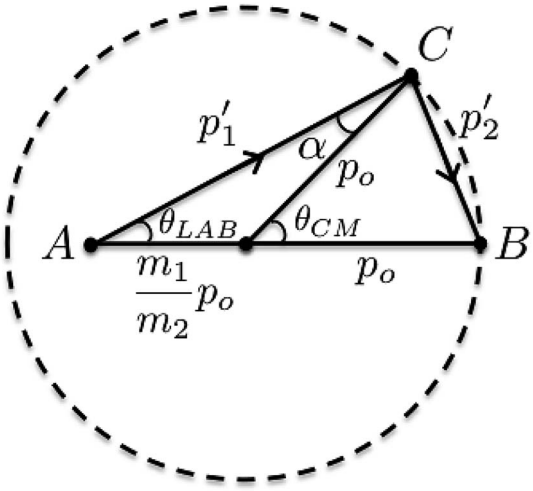

Figure 1. Transformation from LAB→CM frame of reference for particles of different mass.

The transformation is established by obtaining an analytical expression (if possible) for the term on the far right-hand side of equation (5). The relationship between θ_{LAB} and θ_{CM} may be determined by considering the schematic of scattering of two particles A and B in the center-of-mass (CM) frame of reference shown in Figure 1. If the particle B is considered to be at rest in the laboratory frame of reference, then the point B lies on the dashed circle with a radius $p_0 = \mu v$, where $\mu = m_1 m_2/(m_1 + m_2)$ is the reduced mass and $v = v_1 - v_2$ is the relative velocity prior to collision. In the case when $m_1 = m_2$, both A and B lie on the dashed circle, and it is straightforward to show that the relationship between θ_{LAB} and θ_{CM} is as follows:

$$\theta_{CM} = 2\theta_{LAB} \tag{6}$$

resulting in the differential cross section transformation for direct or (resonant) charge transfer collisions:

$$\frac{d\sigma(\theta_{LAB})}{d\Omega_{LAB}} = 4\cos\theta_{LAB}\frac{d\sigma(\theta_{CM})}{d\Omega_{CM}} \tag{7}$$

In the gas mixture, it is necessary to account for cases where $m_1 \neq m_2$. To simplify the analysis, we assume that $v_1 \gg v_2$ such that the second particle is at rest, and point B thus lies on the dashed circle as in Figure 1. This is a reasonable assumption at GEO, since the H^+ are approximately 1 keV, and the hydrazine chemical species are characterized by energies of less than 1 eV. Following this approach then, we have that m_1 corresponds to m_{H^+}, and $m_1 < m_2$ regardless of the collision partner for all chemical species in the hydrazine mixture, as shown in Figure 1.

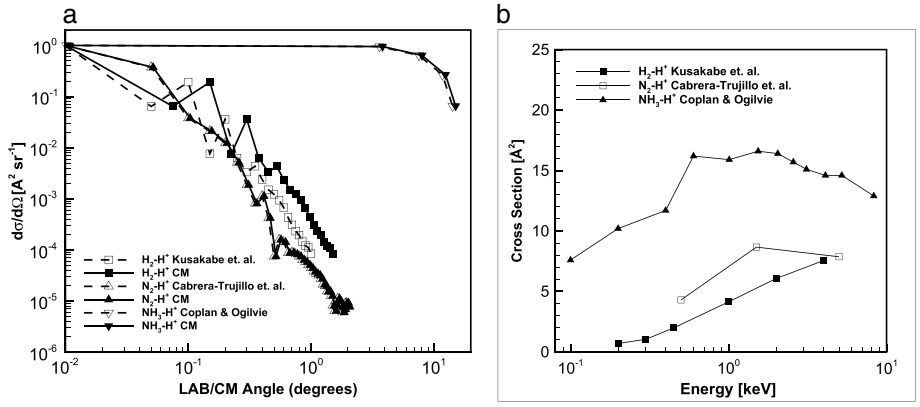

Figure 2. (a) Differential cross sections (DCS) and (b) total cross sections (TCS) for collision dynamics of $H_2/N_2/NH_3 - H^+$ system.

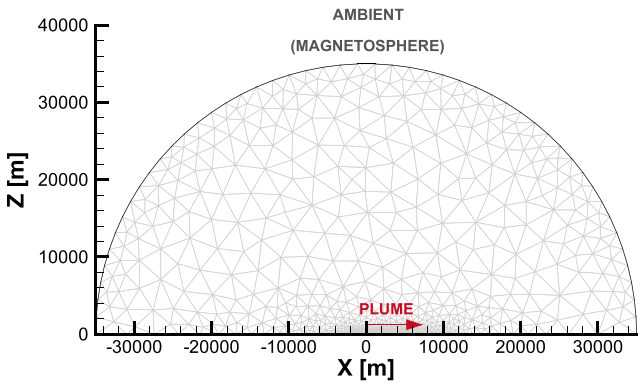

Figure 3. DSMC/PIC computational domain. Axis of symmetry lies along the *x* axis, and the nozzle exit plane is located at the origin. Red arrow indicates the plume flow direction, and geomagnetic field lines are aligned with the *z* axis.

Invoking the sum of angles and law of sines, we can establish the relationship between the scattering angle of particle 1 (H^+ in this case) in the LAB frame (θ_{LAB}) and the CM frame (θ_{CM}) and finally the expressions for $\sin\theta_{LAB}$ and $d\theta_{LAB}$ which are required for the transformation:

$$\theta_{CM} = \theta_{LAB} + \sin^{-1}\left(\frac{m_1}{m_2}\sin\theta_{LAB}\right) \tag{8}$$

$$d\theta_{CM} = 1 + \frac{m_1/m_2\cos\theta_{LAB}}{\sqrt{1-\left(m_1/m_2\right)^2\sin^2\theta_{LAB}}} \tag{9}$$

$$\sin\theta_{CM} = \sin\left[\theta_{LAB} + \sin^{-1}\left(\frac{m_1}{m_2}\sin\theta_{LAB}\right)\right] \tag{10}$$

The transformation can be made by expressing the right-hand side of equation (5) in terms of θ_{CM} and then plotting the CM DCS as a function of θ_{CM}. However, equations (8)–(10) can only be solved approximately using an iterative solution approach, so an immediate analytical form is not possible. If instead the right-hand side is left in terms of θ_{LAB}, the final LAB → CM transformation is expressed as follows:

$$\frac{d\sigma(\theta_{CM})}{d\Omega_{CM}} = \frac{\sin\theta_{LAB}}{\sin\left[\theta_{LAB} + \sin^{-1}\left(\frac{m_1}{m_2}\sin\theta_{LAB}\right)\right]\left(1 + \frac{m_1/m_2\cos\theta_{LAB}}{\sqrt{1-(m_1/m_2)^2\sin^2\theta_{LAB}}}\right)}\frac{d\sigma(\theta_{LAB})}{d\Omega_{LAB}} \tag{11}$$

The right-hand side is evaluated with a value for the LAB DCS and the corresponding angle θ_{LAB} (from experimental data), and finally, the transformed value for the CM DCS is obtained. These values are plotted against θ_{CM}, which is determined for each value of θ_{LAB} from equation (8). This transformation is applied to the differential cross sections describing the postcollision scattering of $H_2 - H^+$, $N_2 - H^+$, and $NH_3 - H^+$ collision partners in the center-of-mass frame of reference, and the resulting cross sections are plotted in Figure 2a. The LAB→CM transformation is most prominent for cases in which the collision partners are of equal mass ($m_1 = m_2$), and the differential cross section in the CM frame of reference approaches the LAB frame value when $m_1 << m_2$. Total direct (nontransfer) and charge transfer cross sections employed in this model are reported in the literature for the mixture constituents [*Kusakabe et al.*, 2000; *Cabrera-Trujillo et al.*, 2002; *Coplan and Ogilvie*, 1970], and the charge transfer cross sections are shown in Figure 2b.

Table 2. Thruster Exit Plane Conditions and Ambient Flow Conditions

Species	m (kg kmol^{-1})	k_bT/q_o(eV)	V (m s^{-1})	n (m^{-3})
H_2	2.02	0.03	1900	3.99×10^{23}
N_2	28.0	0.03	1900	1.74×10^{22}
NH_3	17.0	0.03	1900	1.99×10^{22}
H^+	1.01	1.0×10^3	0	3.0×10^6

Table 3. Larmor Radius (With *B* Field Variation)

Species	Mean (km)	Variation (+/−)
r_{L,H_2}	0.4	0.30/0.46
r_{L,N_2}	5.6	4.2/6.5
r_{L,NH_3}	3.3	2.6/4.0

2.3. Magnetic Field Model

In addition to CEX and photoionization interactions, charged particles in GEO are subject to interaction with Earth's magnetic field. Previous studies in the LEO environment have demonstrated the important role that the magnetic field plays in the propagation of the ion plume. The magnetic field strength at GEO, however, is considerably weaker, and the spacecraft on average is stationary with respect to the field lines. The magnetic field model employed in this work is adopted from previous studies at low Earth orbit and has been extended for plasma mixtures. The gyroscopic motion of the charged particles is dependent upon the ion mass through the Larmor radius, r_L, and the gyration frequency, ω_L, which are determined according to

$$r_L = \frac{V_{x0}^{\text{ion}}}{\omega_L}, \tag{12}$$

$$\omega_L = \frac{q^{\text{ion}} B}{m^{\text{ion}}}. \tag{13}$$

In equation (12), V_{x0}^{ion} is the initial x-velocity of the $H_2^+/N_2^+/NH_3^+$ species entering the gyroorbit, which is equivalent to the postcollision x-velocity after a charge exchange reaction. In equation (13), q^{ion} is the fundamental charge, B is the magnetic field strength, and m^{ion} is the molecular mass of the $H_2^+/N_2^+/NH_3^+$ species.

The magnetic field lines in these simulations are assumed to be perpendicular to the thrust vector (aligned with the x direction). A full outline of the magnetic field model is presented in *Stephani and Boyd* [2014]. The significance of the magnetic field interaction with the charged hydrazine plume species, H_2^+, N_2^+, and NH_3^+, was established by investigating magnetic field strengths of B = 1.1×10^{-7} T (at GEO) and a limiting case of B→ 0. The magnetic field is found to have only a minor influence on the ion plume development and a negligible influence on the neutral plume development for the conditions presented here.

2.4. Plume Configurations

The plume interactions investigated in this study address both steady and unsteady firings of a hydrazine spacecraft thruster into the ambient magnetosphere free stream in GEO. The spacecraft thruster is located at the origin $(x, z) = 0$ and generates thrust in the $-x$ direction. The plume flow is simulated on an axisymmetric computational domain with a radius of 35 km, which is shown in Figure 3. The plume flow at the thruster exit is in the $+x$ direction, as indicated by the red arrow. A mass flow rate of $\dot{m} = 5.0 \times 10^{-4}$ kg/s is specified through an inflow boundary condition at the nozzle exit plane (not visible in Figure 3). The exit plane flow is modeled as a neutral propellant mixture of molecular hydrogen, nitrogen and ammonia, with the properties shown in Table 2. The computational frame of reference is held fixed with respect to the spacecraft thruster, so the ambient H^+ ions follow a thermal distribution in this frame of reference. Recalling discussion of the magnetic

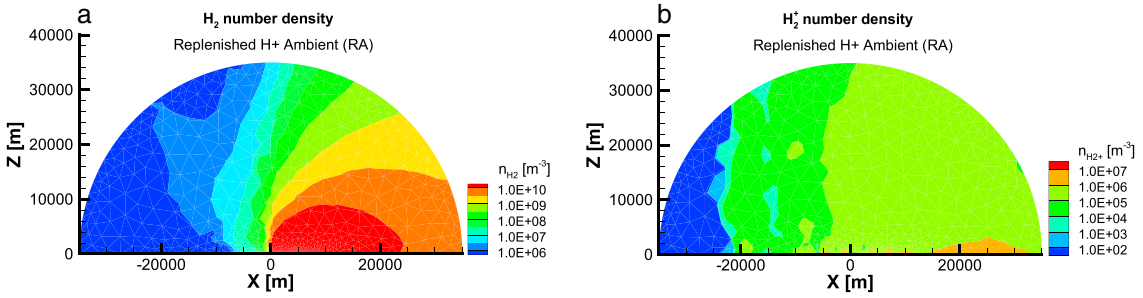

Figure 4. Contours of (a) H_2 number density and (b) H_2^+ number density for charge exchange with a replenished ambient (RA). The lower saturation limit on the contour levels corresponds to the ambient density. Note the difference in the contour level upper limits.

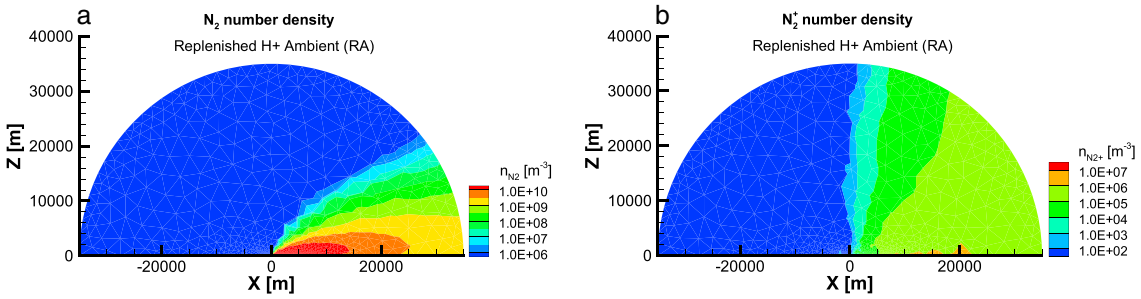

Figure 5. Contours of (a) N_2 number density and (b) N_2^+ number density for charge exchange with a replenished ambient (RA). The lower saturation limit on the contour levels corresponds to the ambient density. Note the difference in the contour level upper limits.

field model, the geostationary magnetic field lines are assumed to be aligned vertically along the $+z$ axis in the computational domain and are assumed to be stationary relative to the spacecraft thruster.

Typical values of the spacecraft propellant ion gyroscopic radii are summarized in Table 3, based on a nominal magnetic field strength of $B = 1.1 \times 10^{-7}$ T including diurnal variation [*Rufenach et al.*, 1992]. Properties of temperature, velocity, and number density are specified for the ambient species (H^+) throughout the domain at the start of the simulation and at the inflow boundary for the neutral chemical species.

3. Results

Simulation results from both steady and unsteady thruster burns are presented in this section. The first case that is presented examines the ion and neutral steady plume development without photoionization, such that the ion plume is formed from spacecraft neutral charge exchange collisions with the ambient H^+. Recall that charge transfer between spacecraft neutrals and ambient ions effectively depletes the local ambient plasma density, and the ambient plasma is assumed to be replenished at a finite rate based on the time-of-flight of 1 keV H^+ ions from the ambient reservoir at −20 km. As shown in Figures 4a and 7a, this is the approximate location at which the neutral plume density drops below the ambient density. The second case incorporates both charge exchange and photoionization processes to compare the relative importance of these mechanisms on the formation of the ion plume. Finally, it is important to note that only the $H_2^+/N_2^+/NH_3^+$ ions are influenced by the electrostatic and magnetic field forces; any influence of these forces on the motion of the neutral $H_2/N_2/NH_3$ particles is a result of secondary charge-exchange interactions, in which a neutral particle becomes magnetized through charge exchange, interacts with the magnetic field, and then becomes demagnetized through a charge-exchange collision.

The second set of simulation results examine an unsteady thruster firing, in which the thrusters are fired for 2 s and then turned off. The evolution of both the neutral and ion plumes is examined during and after the thruster burn to determine the rate of dissipation of each chemical species from the computational domain.

3.1. Plume Development With Replenished Ambient

The steady state flow field in the replenished ambient (RA) case is presented in Figures 4–6. The contours in Figures 4–6a show the number density of the hydrazine neutrals which are emitted in the $+x$ direction from

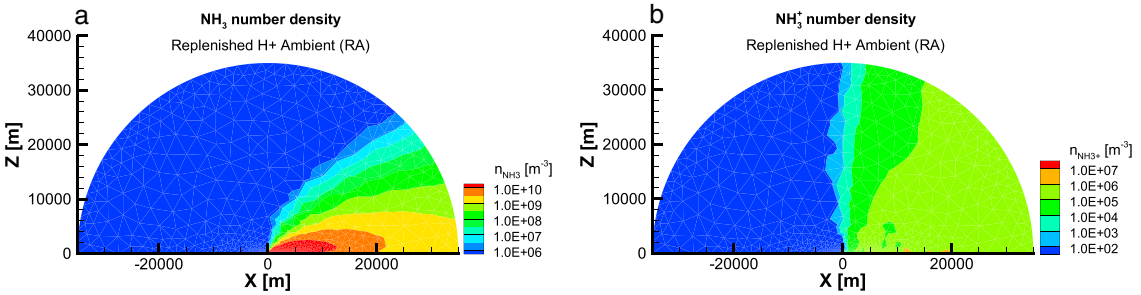

Figure 6. Contours of (a) NH_3 number density and (b) NH_3^+ number density for charge exchange with a replenished ambient (RA). The lower saturation limit on the contour levels corresponds to the ambient density. Note the difference in the contour level upper limits.

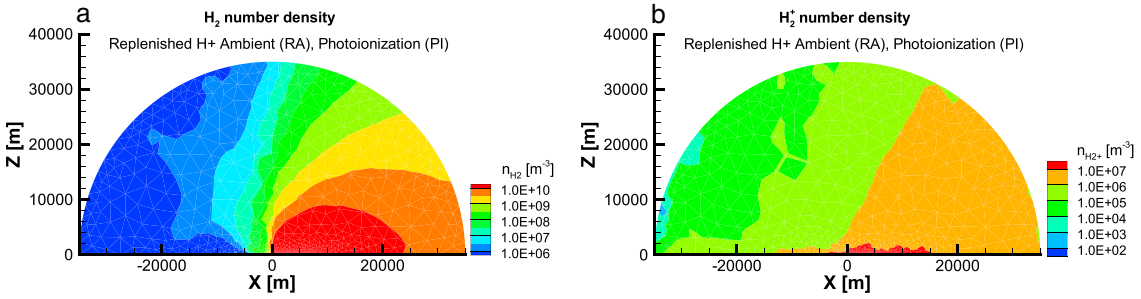

Figure 7. Contours of (a) H_2 number density and (b) H_2^+ number density for photoionization (PI) with a replenished ambient (RA). The lower saturation limit on the contour levels corresponds to the ambient density. Note the difference in the contour level upper limits.

the nozzle exit. The plume undergoes a strong expansion into the rarefied ambient plasma environment, and these particles interact through MEX and CEX collisions with the ambient ions and with neutral plume particles. The number density of the corresponding spacecraft ions generated through charge exchange are shown in Figures 4–6b. Both neutral and ion plumes undergo expansion in the near-vacuum ambient, and the ion plume is also subject to forces from the electric and magnetic fields.

Examination of the neutral and ion plumes in Figures 4–6 reveals the influence of the self-consistent electrostatic field on the ion plume. The neutral chemical species plume undergoes considerable expansion, but the plume generally propagates in the $+x$ direction. The plume concentrations in the farfield remain orders of magnitude higher than the ambient density, which is represented by the lower saturation of the contour levels at 1.0×10^6 m^{-3}. Owing to the plume composition and relatively small molecular mass, the H_2 plume shows the greatest extent, while the N_2 and NH_3 plumes are at lower concentrations.

The corresponding ion plumes are significantly lower in density, and the ion plume concentration is limited to values near or below the ambient density. This is due to the depleting nature of the H^+ ions from charge exchange collisions; the finite-rate replenishing of the ambient ions in the path of the neutral plume is significantly longer than the charge exchange collision frequency between the neutral particles and ambient ions. As a result, the ion plume concentration in this case is limited by the ambient ions available for charge exchange.

The evolution of the ion plumes indicates a strong influence of the electric field on the charged chemical species. The acceleration due to the electrostatic forces drive the ions away from the thruster origin, both in the upstream ($-x$ and H_2^+ only) and downstream ($+x$) directions. In each case, the ion plume concentration is significantly higher in the downstream direction; this is attributed to the higher concentration of neutral plume chemical species downstream available for ion plume production. The significant spread of the ion plume however underscores the influence of the electrostatic field on the ion plumes.

3.2. Plume Development With Photoionization

The steady state flow field generated with a replenished ambient (RA) and photoionization (PI) is presented in Figures 7–9a and Figures 7–9b. The contours in Figures 7–9a again show the hydrazine neutral number density. Recall that in this case the spacecraft neutrals may undergo charge exchange with the ambient H^+

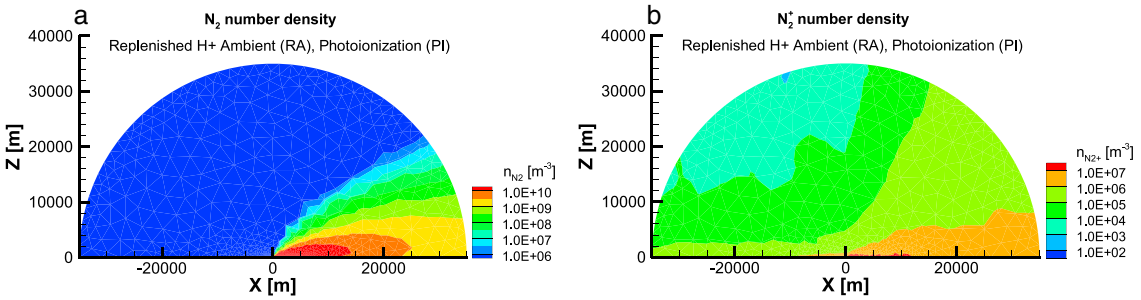

Figure 8. Contours of (a) N_2 number density and (b) N_2^+ number density for photoionization (PI) with a replenished ambient (RA). The lower saturation limit on the contour levels corresponds to the ambient density. Note the difference in the contour level upper limits.

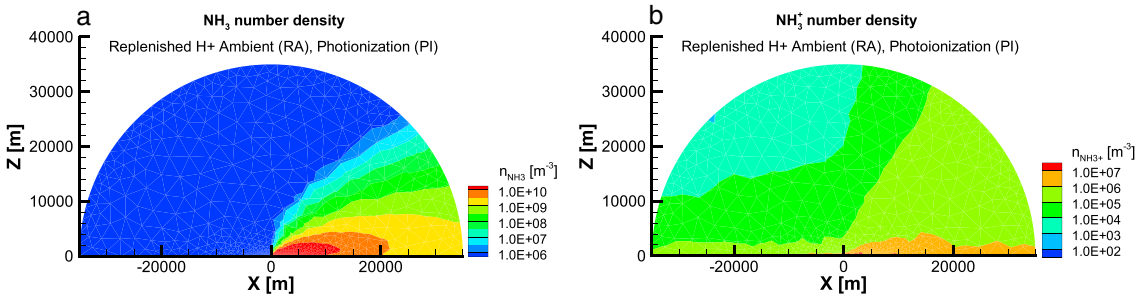

Figure 9. Contours of (a) NH_3 number density and (b) NH_3^+ number density for photoionization (PI) with a replenished ambient (RA). The lower saturation limit on the contour levels corresponds to the ambient density. Note the difference in the contour level upper limits.

ions and may also undergo photoionization. The number density of the spacecraft ions generated through charge exchange is shown in Figures 7–9b. The neutral plume development is nearly identical to the plumes presented in the previous section and develop largely in the $+x$ direction. The ion plumes, however, show a significant increase in concentration owing to the additional ion production through photoionization. Although the majority of the N_2^+ and NH_3^+ ion plumes remains at a concentration below the ambient density, the H_2^+ ion plume has a high-density core that extends 15 km downstream of the thruster origin.

A quantitative comparison of the results from Figures 5 to 9 is presented in Figure 10a–10c. These figures show the number density of the spacecraft neutrals (H_2,N_2, and NH_3) and ions (H_2^+,N_2^+, and NH_3^+) along the plume centerline, starting from the thruster exit, in the $+x$ direction. The solid lines indicate the number density of the spacecraft neutrals as a function of distance from the thruster, and the dashed lines represent the spacecraft ions. Number density profiles are shown for three distinct simulation cases: (1) RA, the replenished ambient case, (2) PI, the Photoionization case including replenished ambient (both presented above), and (3) FA, the fixed ambient case (not repsented above). The fixed ambient case assumes that the ambient H^+ ions are replenished at an infinite rate, providing a fixed ambient density for charge exchange processes throughout the simulation. It is observed in these comparisons that photoionization has a significant impact on the ion plume concentration, increasing the ion plume density by approximately 1 order of magnitude. As shown by this comparison, the increase in ion concentration is approximately equivalent to assuming an infinite replenishing rate (or fixed ambient) for the ambient ions.

3.3. Unsteady Plume Simulations

Plume simulation results are presented next which examine an unsteady thruster plume firing for 2 s, after which the thrusters are turned off. The thrusters fire in the $+x$ direction, and the neutral plume expands in the near-vacuum ambient while undergoing charge exchange and photoionization. The simulation results show the convection and eventual dissipation of the neutral and ion plumes to levels below the ambient density of approximately 1×10^6 m^{-3} for each of the chemical species. Each column in Figure 11 represents the time evolution of the neutral plumes (black contour lines) and the ion plumes (red contour lines), starting at 2 s

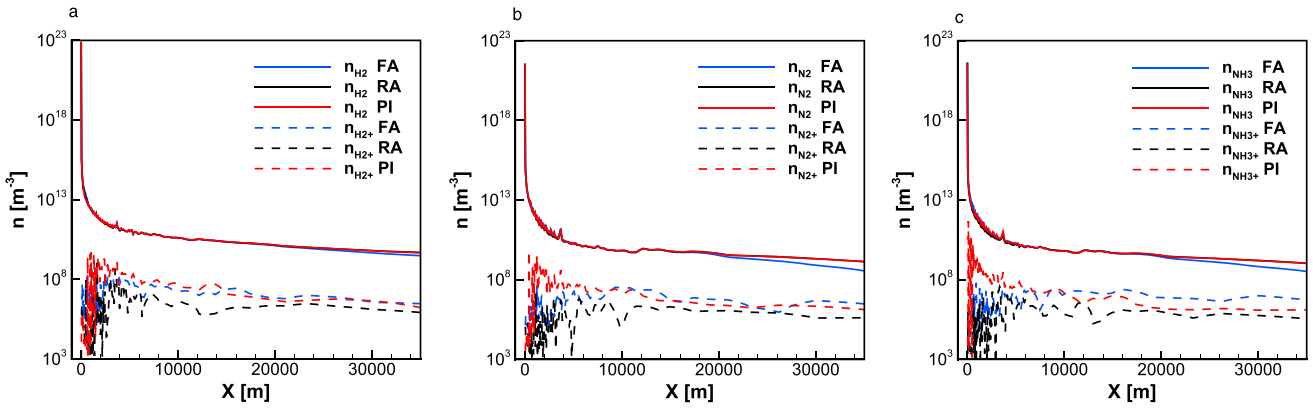

Figure 10. Plots of (a) H_2/H_2^+, (b) N_2/N_2^+ number density, and (c) NH_3/NH_3^+ number density for fixed ambient (FA), replenished ambient (RA), and photoionization (PI) with a replenished ambient (RA) along the plume centerline as a function of x.

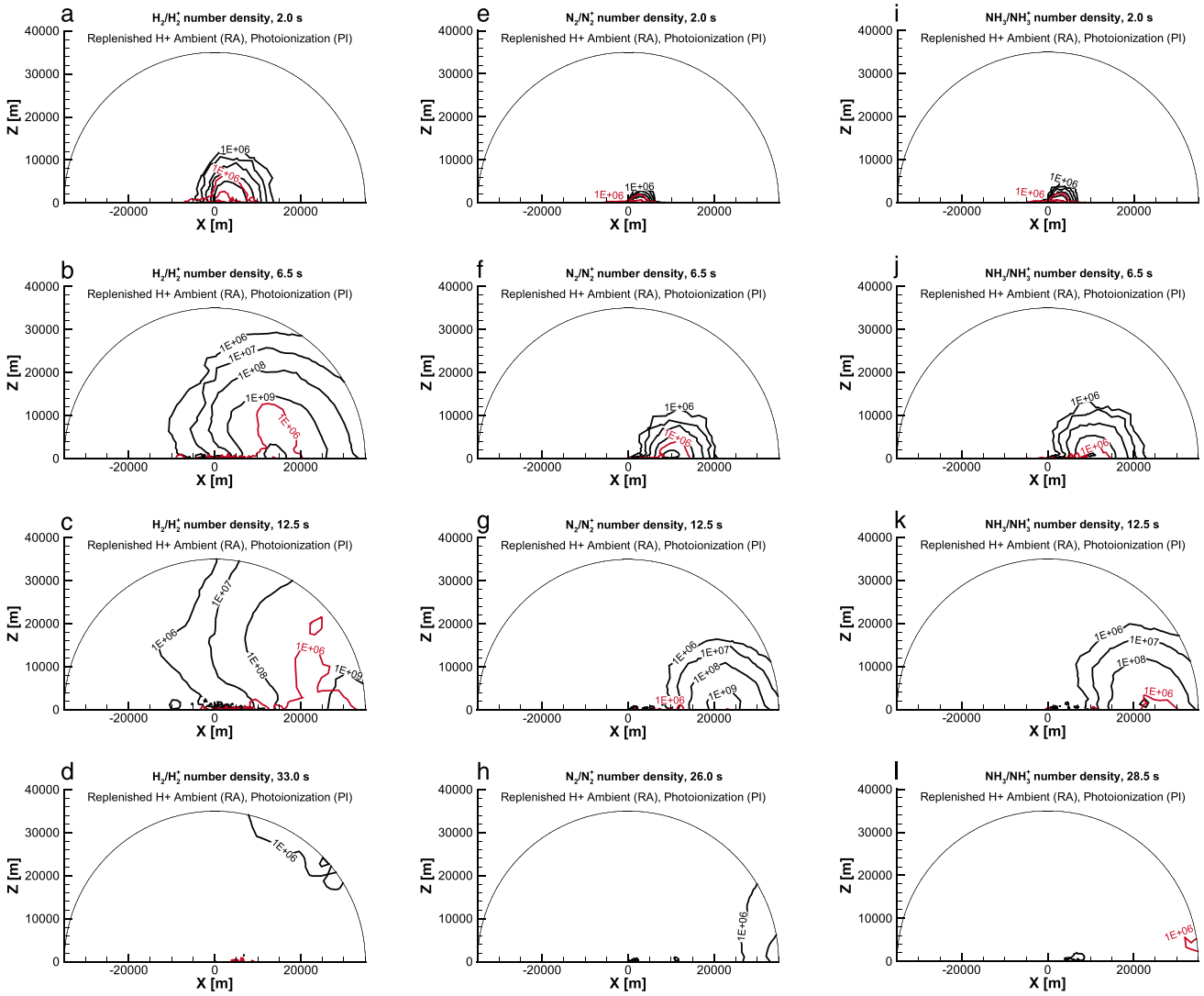

Figure 11. Time evolution of neutral and ion plumes during an unsteady thruster firing with B = 1.1×10^{-7} T, with replenishing and photoionization. Thrusters are fired for (a, e, and i) 2.0 s and then turned off. The lightest of the species, H_2, exhibits the greatest plume diffusion, while the heaviest of the species, NH_3, convects out of the computational domain first.

(a, e, and i) and stepping through time up until the majority of the plume has convected out of the domain (d, h, and l).

The total time required for the neutral and ion plumes to dissipate to levels below the ambient density everywhere (±35 km from the spacecraft) is approximately 34 s. The core of the neutral plume (the highest density region) leaves the computational domain after approximately 15 s, which is the time required for a plume traveling at the thruster exit velocity of 1900 m/s to reach the edge of the computational domain. As the plume is composed of chemical species which vary in molecular weight, the lighter plume species are faster, and the core of the H_2 plume reaches the edge of the domain first, followed by the NH_3, and then the N_2 plume core. This "time of flight" is nearly half of the total dissipation time. The additional time required for dissipation is largely a result of the plume expansion, as well as collisional effects near the thruster exit. These mechanisms work to decrease or reverse the plume neutral particle velocities such that the edges of the plume remain within the computational domain for an extended period after the core of the plume has already vanished. It is found that the N_2 plume vanishes completely (below the ambient number density levels) first, after approximately 26 s, while the H_2 is the final chemical species to dissipate completely.

4. Conclusions

The focus of this work was to examine the development of spacecraft neutral and ion plumes during steady and unsteady hydrazine thruster burns. The plume was modeled as a gas mixture composed of the primary hydrazine postcombustion products, consisting of H_2, N_2, and NH_3, subject to interaction with the ambient H^+ ions in the magnetosphere and photoionization. Detailed differential and total cross sections were used to model the formation of spacecraft ions formed during charge exchange (CEX) interactions with ambient ions in the magnetosphere plasma. This work also established the relative significance of the competing mechanisms of charge exchange (H^+ depletion) and ambient replenishing within the plume, as well as photoionization processes. Both steady and unsteady spacecraft neutral and ion plume results were presented.

The neutral plumes generated from the hydrazine rocket were not strongly influenced by the selection of the ionization mechanisms (i.e., charge exchange with or without photoionization), as the neutral plume densities and general shapes were nearly identical in the two cases. The ion plumes, however, showed a significant increase in both concentration and extent, when photoionization is included. The concentration along the plume centerline was increased by approximately 1 order of magnitude, which was found to be approximately equivalent results employing the fixed ambient model (infinite replenishing rate) without photoionization.

The unsteady simulation of the 2 s thruster burn examined the relative neutral and ion plume convection and dissipation at large distances (±35 km) from the spacecraft. The ion plume, although present at lower concentrations, closely tracked the high-density neutral core. The densities drop to values below the ambient, with only traces of low H_2 plume concentrations ($\mathbf{O}(10^6)$ m^{-3}) near the plume centerline after 33 s.

Acknowledgments
The support of Air Force Research Laboratory (AFRL) Space Vehicles Directorate and Barron Associates, Inc. for this work under subcontract FA9453-11-C-0181 is gratefully acknowledged. The authors are also grateful for the helpful suggestions by the reviewers. Information regarding the simulation results presented in this paper may be obtained from K. Stephani. Computational resources and technical support were provided by the CAEN Advanced Computing Center at the University of Michigan and by the Texas Advanced Computing Center through a National Science Foundation XSEDE award.

References

Alexeenko, A., D. Wadsworth, S. Gimelshein, and A. Ketsdever (2004), Numerical modeling of ISS thruster plume induced contamination environment, in *SPIE 49th Annual Meeting, Optical System Contamination: Effects, Measurements and Controll VII Conference (AM405)*, edited by J. C. Fleming, M. G. Dittman, and P. T. C. Chen, pp. 125–136, SPIE, Bellingham, Wash.

Bernhardt, P., et al. (2012), Ground and space-based measurement of rocket engine burns in the ionosphere, *IEEE Trans. Plasma Sci.*, *40*(5), 1267–1286.

Bird, G. (1994), *Molecular Gas Dynamics and the Direct Simulation of Gas Flows*, Oxford Univ. Press, Oxford, U. K.

Birdsall, C., and A. Langdon (2004), *Plasma Physics Via Computer Simulation*, Taylor and Francis, New York.

Burke, W., L. Gentile, J. Machuzak, D. Hardy, and D. Hunton (1995), Energy distributions of thruster pickup ions detected by the Shuttle Potential and Return Electron Experiment during TSS 1, *J. Geophys. Res.*, *100*(A10), 19,773–19,790.

Cabrera-Trujillo, R., Y. Ohrn, E. Deumens, J. Sabin, and B. Lindsay (2002), Theoretical and experimental studies of the H+-N2 system: Differential cross sections for direct and charge-transfer scattering at kilo-electron-volt energies, *Phys. Rev. A*, *66*, 042712.

Cai, C. (2005), Theoretical and numerical studies of plume flows in vacuum chambers, PhD Dissertation, Univ. of Michigan, Ann Arbor, Mich.

Coplan, M., and K. Ogilvie (1970), Charge exchange for H+ and H2+ in H20, CO2, and NH3, *J. Chem. Phys.*, *52*, 4154.

Drakes, J., and D. Swann (1999), DSMC computations of the progress-M spacecraft retrofiring exhaust plume, AIAA Pap. AIAA-99-0975 presented at 37th Aerospace Sciences Meeting, Reno, Nev., 11–14 Jan.

Kaplan, C., and P. Bernhardt (2010), Effect of an altitude-dependent background atmosphere on shuttle plumes, *J. Spacecr. Rockets*, *47*(4), 700–704.

Karabadzhak, G., Y. Plastinin, B. Khmelinin, V. Teslenko, N. Shvets, J. Drakes, D. Swann, and W. McGregor (1997), Experimentation using the mir station as a space laboratory, AIAA Pap. AIAA-97-0288 presented at 36th Aerospace Sciences Meeting and Exhibit, Reno, Nev., 12–15 Jan.

Kusakabe, T., A. Kensuke, J. Gu, G. Hirsch, R. Buenker, M. Kimura, J. Tawara, and Y. Nakai (2000), Charge-transfer processes in collisions of H+ ions with H2, D2, CO and CO2 molecules in the energy range 0.2-4.0 keV, *Phys. Rev. A*, *62*, 062714.

McMahon, W., R. Salter, R. Hills, and D. Delorey (1983), Measured electron contribution to shuttle plasma environment, AIAA Pap. AIAA-83-2598 presented at Shuttle Environment and Operations Meeting, Washington, D. C.

Ngalande, C., T. Lilly, M. Killingsworth, S. Gimelshein, and A. Ketsdever (2006), Nozzle plume impingement on spacecraft surfaces: Effects of surface roughness, *J. Spacecr. Rockets*, *43*(5), 1013–1018.

Rufenach, C., R. McPherron, and J. Schaper (1992), The quiet geomagnetic field at geosynchronous orbit and its dependence on solar wind dynamics pressure, *J. Geophys. Res.*, *97*(A1), 2101–2116.

Stephani, K., and I. Boyd (2014), Detailed modeling and analysis of spacecraft plume/ionosphere interactions in low Earth orbit, *J. Geophys. Res. Space Physics*, *119*, 2101–2116, doi:10.1002/2013JA019222.

Stephani, K., I. Boyd, R. Balthazor, M. McHarg, B. Mueller, and R. Adams (2014), Analysis and observation of spacecraft plume/ionosphere interactions during maneuvers of the space shuttle, *J. Geophys. Res. Space Physics*, *119*, 7636–7648, doi:10.1002/2013JA019476.

Yim, J., F. Sibé, and N. Ierardo (2014), Plume impingement analysis for the European Service Module Propulsion System, paper presented at 50th AIAA/ASME/SAE/ASEE Joint Propulsion Conference, Propulsion and Energy Forum, Cleveland, Ohio, 28–30 Jul.